

NUMERICAL SIMULATION OF NANOSCALE FIN-FET PHOTODETECTOR FOR OPTIMAL DETECTION OF BIOLOGICAL SIGNALS USING INTERPOLATING WAVELETS

R. Ramesh^{1, *}, M. Madheswaran², and K. Kannan³

¹Department of Electronics and Communication Engineering, M.A.M College of Engineering, Trichy-621105, TamilNadu, India

²Center for Advanced Research, Muthayammal Engineering College, Rasipuram-637408, TamilNadu, India

³Department of Mathematics, SASTRA University, Thanjavur, TamilNadu, India

Abstract—The biosensor design for sensing of biological signals is highly complex for accurate detection. Optimal detection of biological signals is necessary for distinguishing different tissues. This paper proposes a threshold-based detection technique which provides significant improvement in FinFET optical biosensor performance using wavelet coefficients. It uses a simple maximum likelihood (ML) function for detecting the threshold values. In this method, we have considered the different layers of body tissue as a turbid medium. To the best of our knowledge, this method is the first of its kind for classifying different tissues using threshold value of optical signals obtained from the surface potential variations of nanoscale FinFET illuminated by laser source of different wavelengths. By using this method, the point to point variations in tissue composition and structural variations in healthy and diseased tissues could be identified. The results obtained are used to examine the performance of the device for its suitable use as a nanoscale sensor.

Received 25 April 2011, Accepted 17 June 2011, Scheduled 22 June 2011

* Corresponding author: R. Ramesh (ramesh24.dr@gmail.com).

1. INTRODUCTION

The non-invasive methods for monitoring and diagnosis of pathological changes in tissues are of great importance in medical diagnostics and therapeutics. Many novel techniques to improve the process of tumor detection are being developed that differentiate the physical properties between healthy and cancerous tissues [1]. Primary prevention seems impossible because the causes of this disease still remain unknown. Early detection is the key to improving breast cancer prognosis. Many novel techniques to improve the process of tumor detection are being developed that differentiate the physical properties between healthy and cancerous tissues. Ionizing radiation such as X-ray may be used for the diagnosis of skeletal abnormalities. Soft tissue lesions and coronary blood vessels may be diagnosed using angiography [2]. Breast cancers can be detected using mammography and reconstruction of tomographic images, etc. Ultra wide band imaging is used for breast cancer detection uses the dielectric contrast between the normal and cancerous tissues at microwave frequencies [3]. A rotating antenna system is used to create an improved image of the breast for tumor detection [4]. Geometrically and Dielectrically accurate numerical breast phantoms used in the development of robust microwave imaging algorithms have been developed [5]. The microwave based methods uses the differences in dielectric properties of the normal and cancerous breast for detection. Due to the ionizing radiation of these methods, continuous or frequent monitoring is not recommended. Magnetic Resonance Imaging (MRI) and positron emission tomography methods are expensive and require contrast agents, for which many people are allergic. Optical techniques due to their nonionic, noninvasive, inexpensive characteristics emerge as an alternative diagnostic technique [2]. The determination of optical properties of various biological materials is essential for many diagnostic and therapeutic applications of light in medicine. In free-space optics, a laser beam incident on a thick tissue surface, due to mismatch in the refractive index at the air-tissue interface, a part of the laser light is back scattered, whereas the remaining part is absorbed in the tissues [6]. The spatial distribution of backscattered and transmitted components of the laser contains information about the structure, metabolic and physiologic activities of tissues [7]. Optical reflectance imaging of tissues is applied to determine the variation in the internal structure of tissues. Human body consists of layered structures of different tissues having distinct optical properties [8]. It has been shown experimentally and theoretically that the diffused reflectance components scattered from the upper and deeper layers of

tissues appear closer or further from the beam entry point [9, 10]. After undergoing various processes in the tissue, the backscattered photons over the surface help in the analysis and reconstruction of images of the internal structure. A neural network based approach for determination of optical properties of biological properties has been reported [11]. The photosensitivity and the integrated circuit compatibility of Field-Effect Transistors (FETs) have extended potential of these devices for their use as photodetectors [12]. El Hamid et al., [15] presented the 3-D analytical modeling of FinFET including mobile charge term. W. Yang et al., [16] reported the scaling theory of FinFET by 3-D analytical solution of Poisson's equation in channel region. The optical effects on the characteristics of a nanoscale FinFET is reported [23]. Classification of tissues suffers from turbid nature of the biological tissues which degrades the biosensor performance. Error performance bound analysis can yield simple analytical upper bounds or approximations to the bit-error probability [25]. In this paper, the detection scheme of the sensor is altered by optimally calculating a threshold value of surface potential I_D obtained by the self-consistent solution of the Poisson-Schrödinger equation solved by using interpolating Wavelets. In practice, I_D is affected by received signal strength and noise. The likelihood thresholding detection (LTD) requires a less complex receiver and higher throughput when compared to conventional methods, such as conventional symbol-by-symbol detection. It provides a BER performance comparable to symbol-by-symbol detection [24].

2. PHYSICS BASED MODELING

The general FinFETs structure and its geometrical parameters are shown in Fig. 1 [16]. The electrostatic potential in the subthreshold region of nanoscale FinFET under illumination from tissue surface can be described by the 3-D Poisson's equation.

$$\begin{aligned} & \frac{\partial^2 U(x, y, z)}{\partial x^2} + \frac{\partial^2 U(x, y, z)}{\partial y^2} + \frac{\partial^2 U(x, y, z)}{\partial z^2} \\ &= \frac{q[N_a(x, y, z) - n(x, y, z) + p(x, y, z)]}{\epsilon_s} + \Delta n - \Delta Q \end{aligned} \quad (1)$$

where $U(x, y, z)$ is the surface potential at a particular point (x, y, z) , $N_a(x, y, z)$ is the uniform channel doping concentration, q is the electronic charge, ϵ_s is the permittivity of silicon, $p(x, y, z)$ is the hole concentration, Δn is the excess carriers generated per unit volume, ΔQ is the attenuated intensity, $n(x, y, z)$ is the electron concentration [14]. The boundary conditions used for solving Equation (1) is shown in [16].

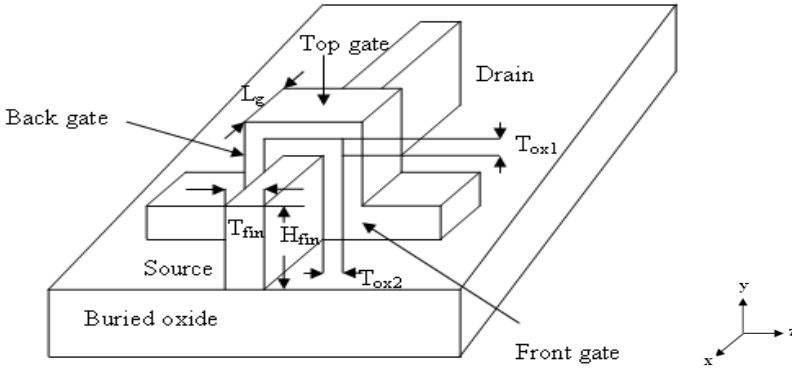


Figure 1. Schematic diagram of FinFET.

The excess carriers generated per unit volume due to the absorption of incident optical power density are given by [13, 23]

$$\Delta n = \frac{1}{W_m} \int_0^{W_m} G_{op}(x) \tau_L dy \quad (2)$$

where W_m is the maximum width of the depletion layer. To determine the optical parameters at each point on the body surface, the following assumptions are made [10].

- (i) the photons incident upon the tissue were considered as neutral particles.
- (ii) the tissue was considered to be a homogenous medium.
- (iii) the beam of photons was considered to be monochromatic.

The incident photon beam profile with each photon of unit intensity (WT_1) is considered. Fig. 2 shows the simulated propagation path of a photon incident on the tissue surface. The simulation process is initiated by launching a light beam, which splits into many photon packets, with initial weight WT_1 and allowed to pass through the biological medium in a given direction. After traveling a distance L in the biological medium, the photon packet is assumed to interact with the medium and a fraction WT_2 of this packet is deposited at the point of interaction after wards a new direction of the photon packet is simulated.

Due to skin tissue-photon interaction, the attenuated intensity considering the refractive index of two media is given by

$$\Delta Q = (WT_1) \left(\mu_a / \mu_t \right) \times \left(\frac{n_2}{n_1} \right) \quad (3)$$

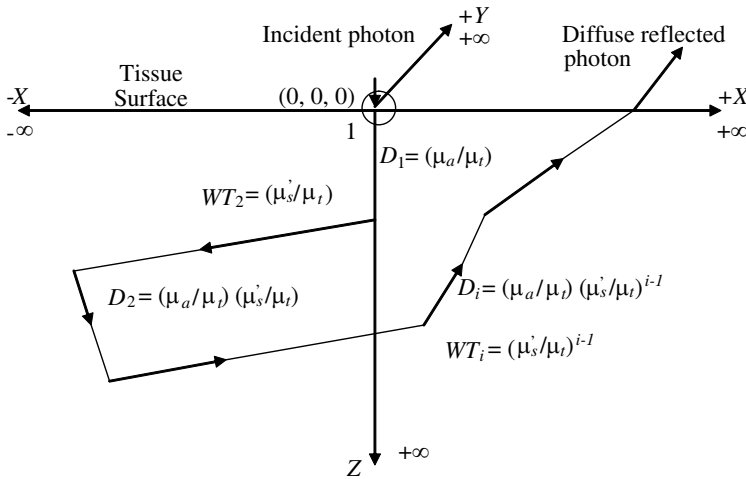


Figure 2. Schematic diagram of photon path in the tissue.

μ_a is the absorption coefficient (cm^{-1}), n_1 is the refractive index of first medium and n_2 is the refractive index of second medium. The total attenuation coefficient is given by

$$\mu_t = (\mu'_s + \mu_a) \tag{4}$$

The reduced scattering coefficient is calculated from

$$\mu'_s = \mu_s (1 - g) \tag{5}$$

The scattering coefficient μ_s and the anisotropy parameter g are combined in the reduced scattering coefficient μ'_s .

In the wavelength band of 600–1300 nm, the absorption coefficient μ_a is approximately $0.1\text{--}10\text{ cm}^{-1}$ and the scattering coefficient μ_s is $100\text{--}1000\text{ cm}^{-1}$ for soft tissues. Typical values of the anisotropy parameter g are between 0.8 and 0.95 for all tissues. The effective attenuation coefficient $\mu_{eff} = \sqrt{3\mu_a\mu_t}$ and the total attenuation coefficient μ_t are the two optical parameters that are used to calculate the reflectance of the tissues.

The path length l in the tissue medium considering the refractive index is given by

$$l = -(\ln R) / \mu_t \times \left(\frac{n_2}{n_1} \right) \tag{6}$$

where R is a random number between 0 and 1.

After passing through a certain distance in the muscle tissue medium, the new photon intensity (WT_2) coming out from the muscle

tissue is calculated by

$$WT_2 = WT_1(\mu'_s/\mu_t) \times \left(\frac{n_2}{n_1}\right) \quad (7)$$

After position 2, the photon is scattered and deflected. The deflection angle θ is calculated by

$$\cos \theta = \frac{1}{2g} \left[1 + g^2 - \left\{ \frac{(1-g^2)}{(1-g+2g\varsigma)} \right\}^2 \right] \quad \text{for } g \neq 0 \quad (8)$$

ς is random number between 0 and 1.

3. BIOLOGICAL TISSUE MODEL

In this paper, the biological tissue is considered to be a turbid medium and it is assumed to be a fading model. The optical signals emerging out of the turbid medium is affected by different types of noise. Hence the tissue is modeled with the noise introduced in the optical signals emerging out of the human body due to diffused reflectance [10].

3.1. Additive Noise

The received signal $i_d[n]$ can be expressed in discrete time n by

$$i_d[n] = h[n]s[n] + i_n[n] \quad (9)$$

where $s[n]$ is the transmitted signal, $h[n]$ is the normalized tissue fading due to the turbid nature of the biological medium and it is assumed to be a constant. $i_n[n]$ is the total additive noise. Although attenuation and scattering can also be included in the model, these do not affect the results when the diffused reflected signal is analyzed stochastically. Assuming the tissue medium is not affected by turbid-induced fading i_n will be the only random variable used in the model. The averaged ML-based bit-error rate for such a medium is expressed in terms of noise and signal parameters. The minimum error probability is provided by the ML-based decision threshold expressed by [26]

$$I_{D,G} = \frac{\sigma_0 I_1 + \sigma_1 I_0}{\sigma_0 + \sigma_1} \quad (10)$$

where σ_1 and σ_0 are the standard deviations of the noise currents for values '1' and '0' designated as healthy and diseased tissues respectively. The threshold value $I_{D,G}$ can be assumed to be a constant if the Gaussian noise is also assumed to be a constant. In Equation (10) $I_1 (= I_0 + 2P_t R)$ and I_0 are averages of the generated currents at the detector for values '1' and '0', respectively, where R is the detector's

responsivity, and P_t is the average of the transmitted power. For simplicity we can assume $2P_tR = 1$. The average signal-to-noise ratio (SNR) with only additive Gaussian noise can be expressed by [24]

$$\gamma_G = \frac{4R^2 P_t^2}{(\sigma_0 + \sigma_1)} \quad (11)$$

3.2. Fading Model

The fading medium coefficient, which models the medium between the transmitter and the biosensor, is given by

$$h = \frac{I}{I_m} = e^{2X}, \quad (12)$$

where I_m and I are the signal light intensities at the transmitter (without turbidity) and biosensor (with turbidity), respectively. Also log-amplitude X is an identically distributed normal random variable with mean μ_x and standard deviation σ_x .

Since variable X is Gaussian, Equation (12) denotes that the expected value of the medium coefficient h is equal to the Gaussian moment-generating function (MGF) evaluated at $X = 2$

$$\mu_I = E[h] = M_x(2) = e^{(2\mu_x + 2\sigma_x^2)} \quad (13)$$

Assuming channel coefficients are independent, the variance of h can be calculated as

$$\sigma_I^2 = E[h^2] - E[h]^2 = M_x(4) - (M_x(2))^2 = e^{(4\mu_x + 4\sigma_x^2)}(e^{4\sigma_x^2} - 1) \quad (14)$$

The average power loss due to turbid fading normalized, such that the fading does not, on average, attenuate or amplify the optical power. We explicitly choose

$$\mu_I = E[h] = 1 \quad (15)$$

which leads us to $\mu_x = -\sigma_x^2$. Thus the variance will be equal to [27]

$$\sigma_I^2 = e^{4\sigma_x^2} - 1 \quad (16)$$

This parameter is called scintillation index (S.I), σ_x is the fading strength, σ_x and varies from 10^{-2} to 1 for different turbidity conditions. Assuming the different layers of body tissue as a lognormal channel medium with additive Gaussian noise, the instant SNR from Equation (11) will be converted to

$$\gamma_L = \frac{4h^2 R^2 P_t^2}{(\sigma_1 + \sigma_0)^2} \quad (17)$$

The averaged value of the SNR can be defined by

$$\bar{\gamma} \triangleq \frac{4R^2P_t^2}{(\sigma_1 + \sigma_0)^2} \quad (18)$$

which is defined same as the expression in Equation (11)

$\Lambda(i_d) > 1$ for '1' bit and $\Lambda(i_d) < 1$ for '0' bit

$\Lambda(i_d) > I_D$ for '1' bit and $\Lambda(i_d) < I_D$ for '0' bit.

4. OPTIMAL DETECTION USING LTD METHOD

In this case, detection performance is highly dependent on the definition of decision metric chosen for the ML function. The ML decision criteria are determined as [26]

$$\Lambda(i_d) = \frac{p(i_d|1)}{P(i_d|0)} \stackrel{1}{<} 1 \quad (19)$$

for any instantaneously received signal i_d . A detection threshold can be defined in such a way that the metric rule is considered as $i_d \ll I_D$. If the root of $\Lambda(i_d) = 1$ is $i_d = I_D$, the probabilities of error for symbols '0' and '1' are calculated by

$$P_e(1|0) = \frac{1}{2} \operatorname{erfc} \left(\frac{I_D - I_0}{\sqrt{2}\sigma_0} \right), \quad (20)$$

$$P_e(0|1) = \frac{1}{\sqrt{32\pi}\sigma_x} \int_0^\infty \frac{1}{h} \exp \left(-\frac{[\ln(h) - 2\mu_x]^2}{8\sigma_x^2} \right) \\ \times \operatorname{erfc} \left(\frac{I_0 - I_D + 2RP_t h}{\sqrt{2}\sigma_1} \right) dh. \quad (21)$$

Assuming equal symbol probabilities, the averaged BER can be calculated using

$$BER_{LTD} = 0.5p_e(0|1) + 0.5p_e(1|0). \quad (22)$$

Clearly I_D providing optimal detection for $\sigma_x = 0.1$ is not applicable for other fading intensities $\sigma_x = 0.2, 0.3, \dots$. So an optimal detection based on threshold finding a threshold value I_D is used.

Based on maximizing the likelihood function $\Lambda(I_D)$ the threshold value for optimal detection is the solution to $\Lambda(I_D) = 1$, which leads to the representation

$$\Lambda(I_D) = \frac{p_e(0|1)}{p_e(1|0)} = 1 \quad (23)$$

Then the final equation becomes

$$\int_{-\infty}^{\infty} \exp\left(-\frac{[X + \sigma_x^2]^2}{2\sigma_x^2}\right) \times \left(\operatorname{erfc}\left(\frac{I_0 - I_D + 2RP_t e^{2X}}{\sqrt{2}\sigma_1}\right) - \operatorname{erfc}\left(\frac{I_D - I_0}{\sqrt{2}\sigma_0}\right)\right) dX = 0. \tag{24}$$

The threshold value for optimal detection is the solution of Equation (24) for I_D , which is only dependent on the fading intensity σ_x and noise statistics. The solution for I_D can be numerically derived utilizing a simple-root finding method.

The LTD method presented in this paper proposes to calculate the threshold value rather than the likelihood ratio, e.g., the symbol-by-symbol method, thus facilitating a less complex receiver design.

The delivered BER by LTD yields

$$BER_{LTD} = \frac{1}{2} \operatorname{erfc}\left(\frac{I_D - I_0}{\sqrt{2}\sigma_0}\right) \tag{25}$$

4.1. Noise and Fading Statistics

The receiver integrates the signal from the photocurrent for each symbol interval. Thus we assume that the noise and fluctuations due to different layers of tissue during symbol intervals can be ignored. However, different symbols face different noise and fading components. Based on Equation (9), the receiver’s output current is calculated by

$$i_p = 2P_t R h + i_n \tag{26}$$

Since the transmitted power for symbol ‘0’ is zero, thus $i_{p,0} = i_n$ for this symbol. I_0 and σ_0 are the average and standard deviation of the received samples of symbol ‘0’ respectively. The random process $i_{p,1}$ is the sum of two independent Gaussian and lognormal variables, i_n and h .

Assuming the turbidity-induced fading coefficients are uncorrelated, the statistics of a received symbol ‘1’ is equal to

$$\mu_{p,1} = \mu_I + I_0, \tag{27}$$

$$\sigma_{p,1}^2 = \sigma_I^2 + \sigma_1^2 = e^{4\sigma_x^2} + \sigma_1^2 - 1 \tag{28}$$

In practice, noise standard deviations σ_0 and σ_1 are very close and can be assumed identical by approximation.

5. MULTIREOLUTION ANALYSIS AND WAVELETS

For semiconductor device simulation using partial differential equations, the grid generation is very important [18]. Grid points must be present accurately approximate to any physical quantity to be measured. The grid layout should be chosen carefully since the computational cost grows with the number of grid points. Finer mesh is needed in doped regions and junctions and coarse mesh in substrate regions. Wavelets with multiresolution approach (MRA) concept are used to achieve this goal [19, 20]. The usefulness of wavelets for solving partial differential equations relies on the definition of MRA [21]. The space of square integral functions on the real line is denoted by $L^2(R)$. The orthonormal basis of wavelets of $L^2(R)$ is formed by dilations and translations of a single function $\Psi(x)$, called a mother wavelet.

$$\Psi_{jk}(x) = 2^{j/2}\Psi(2^jx - k), \quad j, k \in Z. \quad (29)$$

The function $\Psi(x)$ has a companion, the scaling function $\varphi(x)$. They both satisfy the following two-scale relation

$$\varphi(x) = \sum_k a_k \varphi(2x - k), \quad (30)$$

$$\Psi(x) = \sum_k (-1)^k a_{1-k} \varphi(2x - k), \quad (31)$$

where the coefficients a_k ($k = 0, 1, \dots, L-1$) appearing in the two-scale relations (30) and (31) are called the wavelet filter coefficients.

The 3D effective mass Schrödinger equation along the n -channel is given by [17]

$$-\left[\frac{\hbar^2}{2m_x^*} \frac{\partial^2}{\partial x^2} + \frac{\hbar^2}{2m_y^*} \frac{\partial^2}{\partial y^2} + \frac{\hbar^2}{2m_z^*} \frac{\partial^2}{\partial z^2} + qU(x,y,z) \right] \psi_{x,y,z} = E\psi_{x,y,z} \quad (32)$$

In the above equation m_x^* , m_y^* , m_z^* are effective masses in the x , y and z directions. $m_x^* = m_l = 0.916m_0$, $m_y^* = m_t = 0.19m_0$, $m_z^* = m_t = 0.19m_0$. E is the eigen energy, \hbar is the reduced Planck's constant, q is the charge of an electron $U(x,y,z)$ is the surface potential, $\psi(x,y,z)$ is the eigen wave function. The 3-D Schrödinger Equation (32) is solved using the following boundary conditions.

$$\begin{aligned} \psi_{x=0} &= 0, & \psi_{x=L_{eff}} &= 1; & \psi_{y=0} &= 0, & \psi_{y=H_{eff}} &= 0; \\ \psi_{z=-T_{eff}/2} &= 0, & \psi_{z=T_{eff}/2} &= 0 \end{aligned}$$

In this section, the direct solution of 3-D Schrödinger Equation (32) is obtained using Wavelet method. The Interpolating Wavelet

approximation to the solution $\psi_j(x, y, z)$ at scale j is

$$\psi_j(x, y, z) = \sum_{(j,k,l,m) \in I(\eta)} \sum_k \sum_l \sum_m \tilde{c}_{j,k,l,m} 2^{j/2} \phi(2^j x - k) 2^{j/2} \phi(2^j y - l) 2^{j/2} \phi(2^j z - m) \quad k, l, m \in Z \quad (33)$$

where $\tilde{c}_{j,k,l,m}$ are the wavelet coefficients (i.e., they define the solution in wavelet space).

Substituting the wavelet series approximation $\psi_j(x, y, z)$ for $\psi(x, y, z)$ in Equation (32) yields [22]

$$\sum_{(j,k,l,m) \in I(\eta)} \sum_k \sum_l \sum_m \tilde{c}_{j,k,l,m} \left(-\frac{\hbar}{2m_x^*} \frac{d^2}{dx^2} \phi_{jk}(x) - \frac{\hbar}{2m_y^*} \frac{d^2}{dy^2} \phi_{jk}(y) - \frac{\hbar}{2m_z^*} \frac{d^2}{dz^2} \phi_{jk}(z) + (qU_{x,y,z} - E) \phi_{jk}(x) \phi_{jl}(y) \phi_{jm}(z) = 0 \right) \quad (34)$$

To determine the coefficient $c_{j,k,l,m}$, we take the inner product of both sides of Equation (38) with φ_{jn}

$$\sum_{(j,k,l,m) \in I(\eta)} \sum_k \sum_l \sum_m \tilde{c}_{j,k,l,m} \left(-\frac{\hbar^2}{2m_x^*} \right) \int_0^{L_{eff}} \phi_{jk}''(x) \phi_{jn}(x) - \frac{\hbar^2}{2m_y^*} \int_0^{H_{eff}} \phi_{jl}''(y) \phi_{jn}(y) - \frac{\hbar^2}{2m_z^*} \int_0^{T_{eff}} \phi_{jm}''(z) \phi_{jn}(z) + (qU_{x,y,z} - E) \phi_{jk}(x) \phi_{jl}(y) \phi_{jm}(z) \phi_{jn}(z) = 0 \quad n = 2 - N, 3 - N, \dots, 2^j - 1 \quad (35)$$

where prime ' denotes differentiation with respect to the indicated independent variable, L_{eff} is the length of the channel, H_{eff} is the height of the fin, T_{eff} is the thickness of the fin.

Using the notations defined in [23] we write Equation (35) as

$$\sum_{j,k,l,m \in I(\eta)} \sum_k \sum_l \sum_m \tilde{c}_{j,k,l,m} \left(-\frac{\hbar^2}{2m_x^*} \right) (a_{kn}^j + b_{kn}^j + c_{kn}^j) + (qU_{x,y,z} - E) d_{mn}^j = 0; \quad n = 2 - N, 3 - N, \dots, 2^j - 1 \quad (36)$$

The above equations can be put into the matrix-vector form [23]

$$\left(-\frac{\hbar^2}{2m_x^*} \right) (A + B + C) \psi^2 + (qU_{x,y,z} - E) D = 0 \quad (37)$$

Equation (37) can be written as

$$A_1 \psi_{i+1} - A_2 \psi_i + A_1 \psi_{i-1} \quad (38)$$

This system may be easily solved by variety of methods. In this paper, we have used Cholesky's decomposition method. By solving this system, we obtain an accurate solution at resolution level j .

6. COMPUTATIONAL TECHNIQUE

The 3D Poisson's Equation (1) with the boundary conditions under illumination from normal and cancer breast tissues are solved numerically using Leibmann's iteration method to determine the approximate surface potential for a fixed value of gate voltage and assumed value of drain voltage. This value of surface potential is given to the 3D Schrödinger Equation (32). The 3-D Schrödinger equation is solved directly using the boundary conditions by interpolating wavelet method and the exact value of surface potential is obtained for the normal and cancerous breast tissues. The absorption and scattering coefficients are estimated using the surface potential values of the nanoscale FinFET. To aid in the analysis of the performance and effectiveness of the proposed LTD method, this section explains the numerical results obtained from computer simulations.

A schematic diagram of the experimental set up using nanoscale FinFET biosensor for determining the normal and cancerous breast tissues is shown in Fig. 3. The laser light from a compact continuous wave (CW) semiconductor laser with $P_{opt} = 0.5 \text{ W/m}^2$ operating at 532 nm is used. The laser light beam is allowed to fall on the

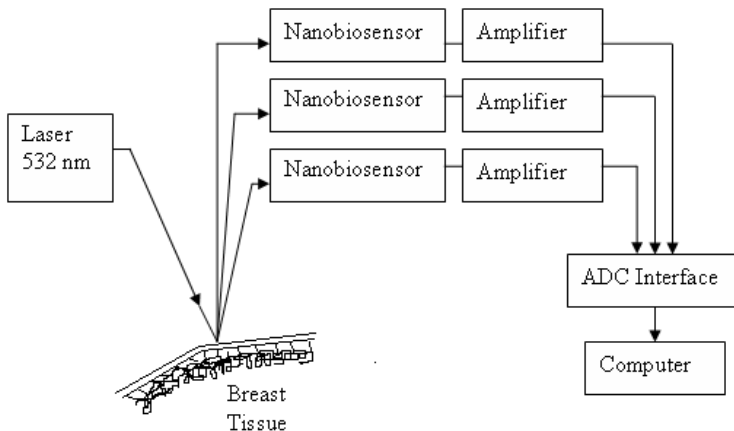


Figure 3. A schematic diagram of the experimental setup using free-space optics.

breast tissue surface. The back-scattered light from the tissue surface is detected by the nanoscale FinFET biosensor and converted into proportional voltage by a set of operational amplifiers. These output values are digitized using a 12-bit analog-to-digital (ADC) converters and are interfaced to a computer for further processing.

7. RESULTS & DISCUSSION

Numerical computation has been carried out for the nanoscale FinFET. The parameters used for the calculation are given in Table 1.

Figure 4 shows the potential profile of the FinFET photodetector under normal illumination using interpolating Wavelet method on a grid of $20 \times 13 \times 10$ points. The surface potential $U(x, y, z)$ is calculated for different values of x and constant values of y and z , ignoring the background dark noise of the device. The figure also shows the illumination results from normal and cancerous breast tissues using the same wavelet method. The surface potential values under illuminated conditions are calculated for $P_{opt} = 0.5 \text{ W/m}^2$ and $V_{DS} = 1.5 \text{ V}$ at 532 nm. It is also found that the surface potential values decreases than the normal illumination when the FinFET is illuminated by the source

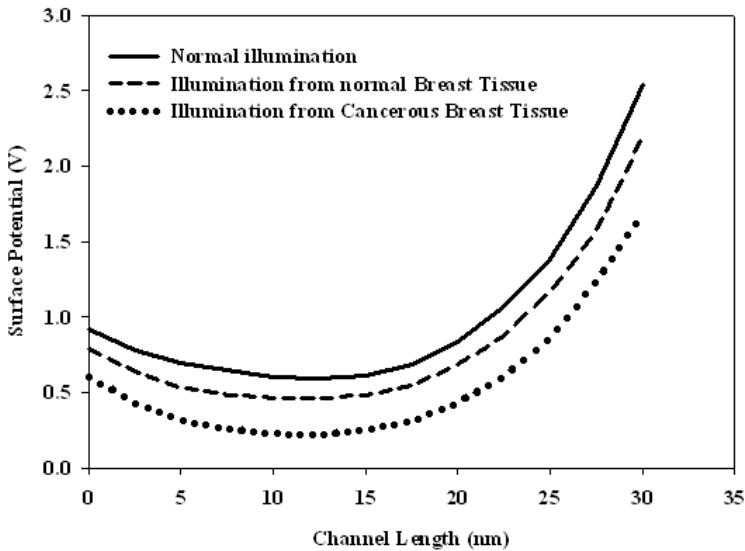


Figure 4. Surface potential calculation along channel length for normal and cancerous breast tissue for $P_{opt} = 0.5 \text{ W/m}^2$ and $V_{ds} = 1.5 \text{ V}$.

Table 1. Parameters and constants.

Parameter	Value
Gate Length (L_g)	30 nm
Top gate oxide thickness (T_{ox1})	5 nm
Front (or) back gate thickness (T_{ox2})	1 nm
Channel Length (L_{eff})	30 nm
Thermal Voltage (V_T)	0.02585 V
Intrinsic carrier concentration (n_i)	$9.65 \times 10^9 / \text{cm}^3$
Acceptor concentration (N_a)	$1 \times 10^{16} / \text{cm}^3$
Flatband voltage (V_{fb})	-0.48 V
Built-in potential (V_{bi})	0.6 V
Gate voltage (V_g)	0.2 V
Wavelength of light source (λ)	476.5, 488, 496.5, 514.5, 532 nm
Refractive index of normal breast tissue (n_1), Cancerous breast tissue (n_2)	1.35, 1.45

of light that arrives from the normal and cancerous breast tissues. The decrease of illumination is more pronounced in the cancerous breast tissue. This is due to the fact that excess carriers generated due to illumination from normal and cancerous breast tissues are very much less than the carriers generated under normal illumination condition and this decreases the conductivity of the channel.

The BER is the key criterion of the performance evaluation of this method. The simulations assume a normalized lognormal fading as $\mu_I = 1$, normalized transmitted power $2RP_t = 1$ and equal noise powers for symbols '0' and '1', $\sigma_0 = \sigma_1$. The noise power is varied to obtain different SNR values. The BER performance for different values of σ_x using the LTD method is shown in Fig. 5. Increasing the SNR does not usually decrease the approximation error. But when the fading intensity σ_x decreases, a decrease of approximation error takes place. The BER performance of the LTD method can be obtained by numerically solving the Equation (25). Any variation in noise power, signal power or fading intensity fundamentally provides a change in BER. Fig. 6 shows a unique I_D for any given medium fading intensity and any given SNR value. The results shows that increasing SNR values results in a decrease of the threshold value, I_D . Assuming a fading strength of $\sigma_x = 0.4$, when the averaged SNR increases from 1 to 17 dB, I_D decreases from 0.52 to 0.34. A similar tendency is observed for different values of σ_x .

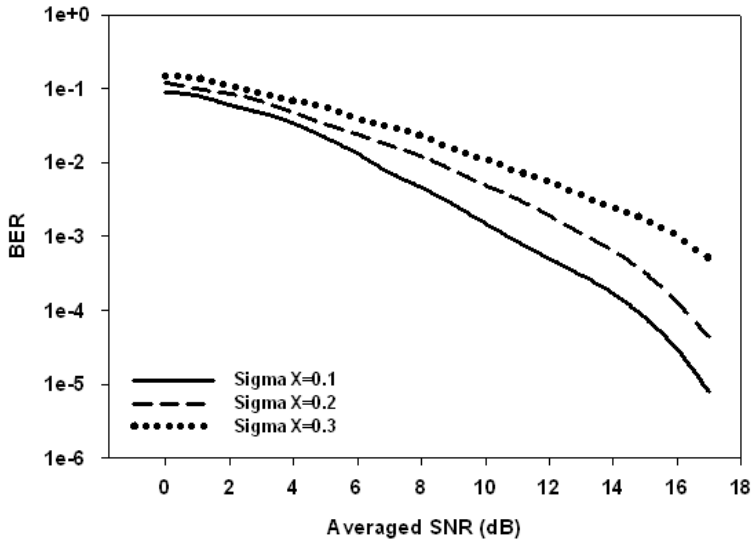


Figure 5. Probability of error using LTD detection method for three different lognormal media.

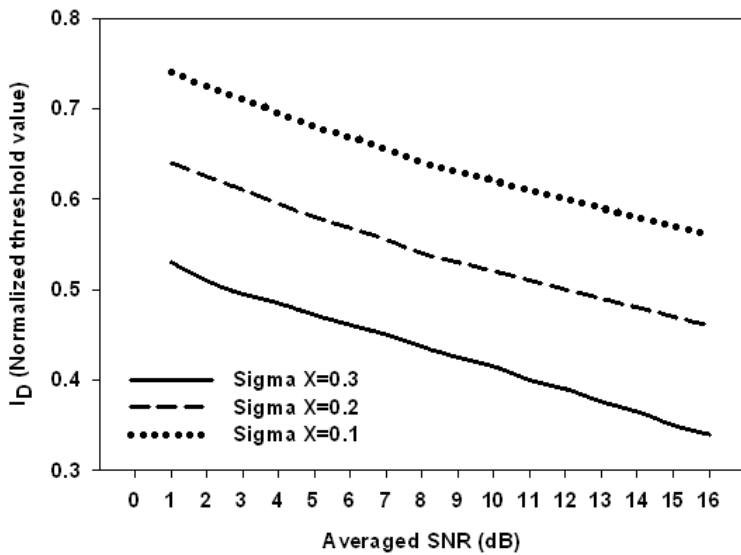


Figure 6. Threshold value of the LTD method with SNR for different values of sigma X.

Figure 7 shows the variation in reflectance with the increase in thickness of the tissue at 532 nm. Initially, this optical parameter increases with increase in thickness of the tissue and attains its maximum value as it reaches the depth of the tissue. This constant value is due to the self absorption of photons within the thickness of the tissue, thus minimizing the influence of tissue reflectance. It is found that the reflectance is lower for the cancerous breast tissue than the normal breast tissue. Fig. 8 shows the variation of absorption of illumination in the normal and cancerous breast tissue. It is also found that the absorption is more pronounced in cancerous tissue than the normal breast tissue. This is due to the fact that the excess carriers generated under illumination are absorbed by the compositional variation of cancerous tissue than the normal breast tissue.

Figure 9 shows the wavelength dependence of the absorption coefficients of both tissues obtained from simulation of the surface potential measurements of nanoscale FinFET using interpolating wavelet. The absorption coefficients are strongly affected by the presence of blood, particularly at wavelengths below 600 nm. The absorption coefficient for normal breast tissue is 2.32/cm at 476.5 nm but increases to 2.75/cm at 488 nm and drops to 2.45/cm at 496.5 nm,

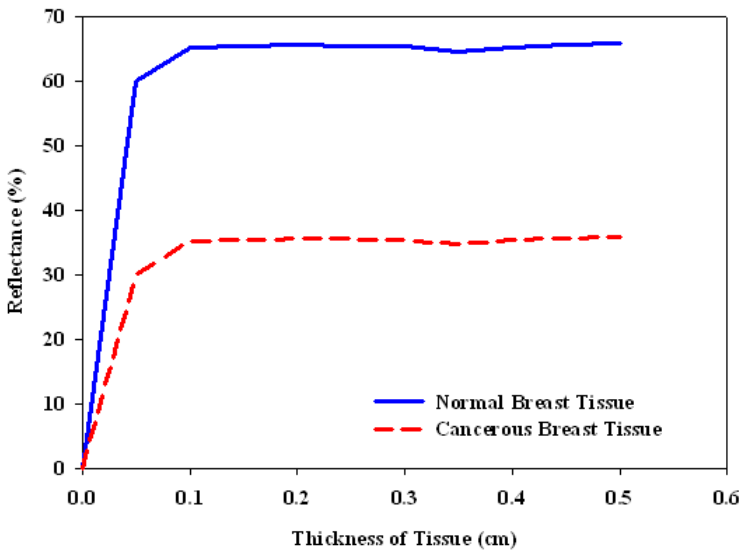


Figure 7. Variation of reflectance for normal and cancerous breast tissue.

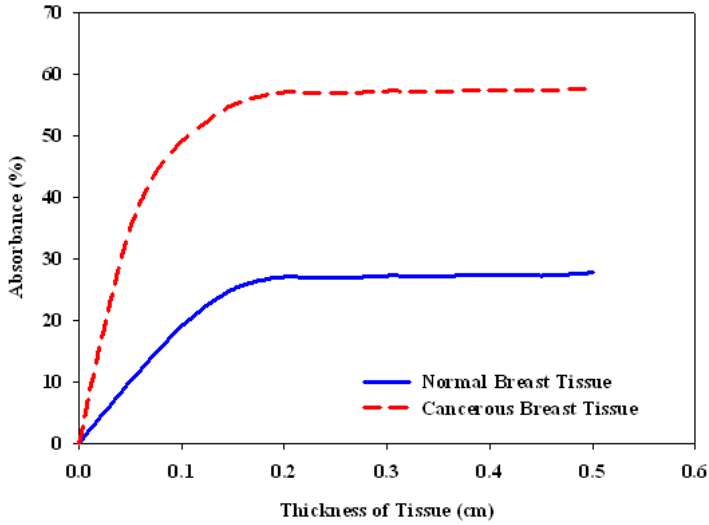


Figure 8. Variation of absorption for normal and cancerous breast tissue.

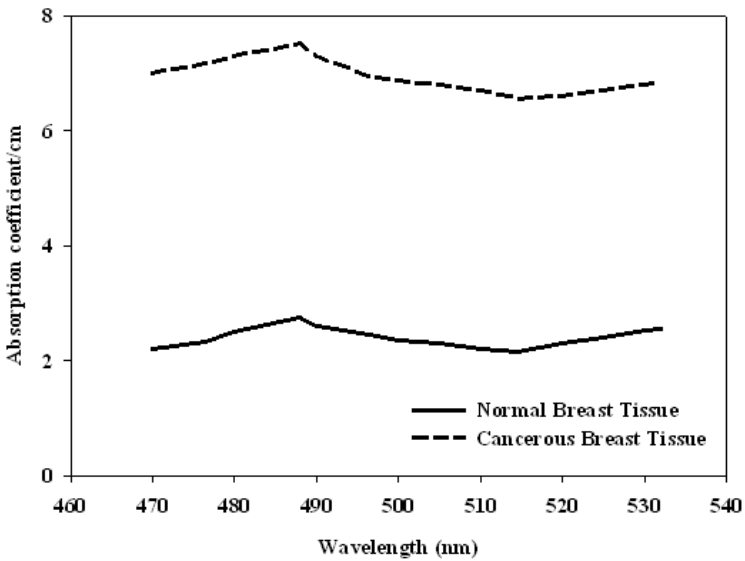


Figure 9. Variation of absorption coefficients Vs wavelengths for normal and cancerous breast tissue.

and to 2.16/cm at 514.5 nm but increases to 2.55/cm at 532 nm, and that for cancerous breast tissue is 7.17/cm at 476.5 nm but increases to 7.51/cm at 488 nm and drops to 6.94/cm at 496.5 nm and to 6.56/cm at 514.5 nm but increases to 6.86/cm at 532 nm. It is found that there were also significant differences in the absorption coefficients between the normal and cancerous breast tissues at the same wavelength. The minimum value of the absorption coefficients for normal breast tissue is 2.16/cm at 514.5 nm and the maximum value is 2.75/cm at 488 nm. The minimum value for cancerous breast tissue is 6.56/cm at 514.5 nm and the maximum value is 7.51/cm at 488 nm.

Figure 10 shows the scattering coefficients for different wavelengths obtained from simulation of nanoscale FinFET using interpolating wavelets. It shows that the scattering coefficient for normal breast tissue is 221/cm at 476.5 nm and drops to 215/cm at 488 nm and to 200/cm at 496.5 nm and to 189/cm at 514.5 nm but increases to 193/cm at 532 nm. It is also clear that there were also significant differences in the scattering coefficients between the normal and cancerous breast tissues. The scattering coefficient for cancerous breast tissue is 333/cm at 476.5 nm and drops to 323/cm at 488 nm and to 316/cm at 496.5 nm and to 298/cm at 514.5 nm but increases to 308/cm at 532 nm. The minimum value of the scattering coefficients for nor-

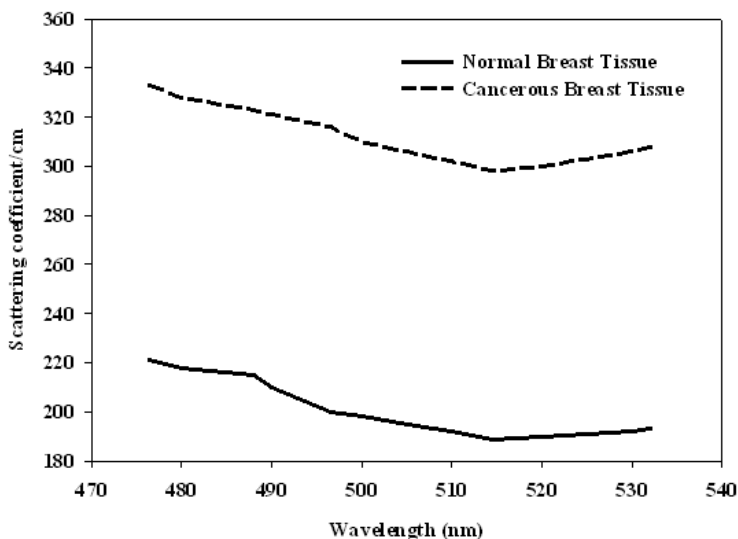


Figure 10. Variation of scattering coefficients Vs wavelengths for normal and cancerous breast tissue.

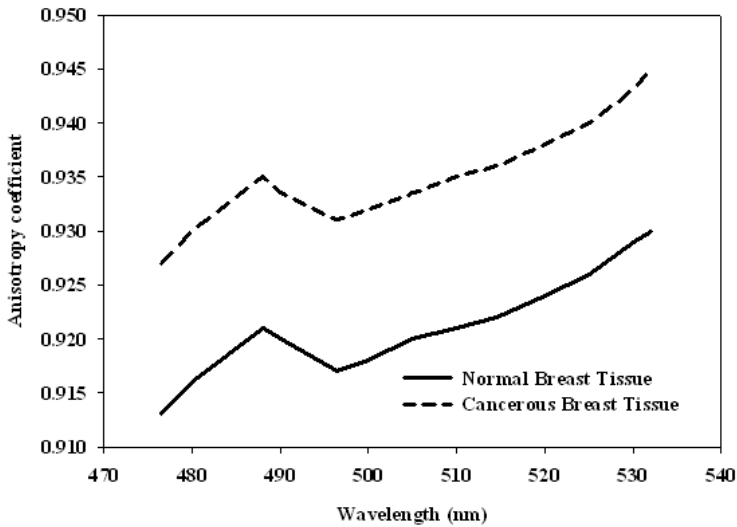


Figure 11. Variation of anisotropy coefficients Vs wavelengths for normal and cancerous breast tissue.

mal breast tissue is 189/cm at 514.5 nm and the maximum value is 221/cm at 476.5 nm. The minimum value of the scattering coefficients for cancerous breast tissue is 298/cm at 514.5 nm and the maximum value is 333/cm at 476.5 nm.

Figure 11 shows the variation of anisotropy coefficients for different wavelengths for normal and cancerous breast tissues. It shows that the anisotropy coefficient for normal breast tissue is 0.913 for 476.5 nm but increases to 0.921 at 488 nm and drops to 0.917 at 496.5 nm but increases to 0.922 at 514.5 nm and to 0.930 at 532 nm. The minimum value of the anisotropy coefficient for cancerous breast tissue is 0.927 at 476.5 nm but increases to 0.935 at 488 nm and drops to 0.931 at 496.5 nm but increases to 0.936 at 514.5 nm and to 0.945 at 532 nm.

8. CONCLUSION

The optimal detection of biophotonic signals in nanoscale FinFET biosensor using wavelet coefficients approach for accurate determining of the optical properties of normal and cancerous breast tissues using nanoscale FinFET shows that the LTD method provides more accurate estimation of BER in body tissues medium. It is found that there is a large difference in the optical parameters between normal and

cancerous breast tissues. It is also found that the optical parameters are wavelength dependent. The LTD method was found to effectively reduce the computational load. However, this method produces a slight loss of BER performance. Thus it provides a trade-off between receiver complexity and BER performance improvement. In the future work, the same characteristics of nanoscale FinFET may be used to characterize the different stages of breast cancer and their optical parameters can be estimated. Neural networks and optimization techniques can also be implemented to extract the needed optical parameters.

REFERENCES

1. <http://www.cancer.org/Research/CancerFactsFigures/CancerFactsFigures/cancer-facts-and-figures-2010>.
2. Srinivasan, R., D. Kumar, and M. Singh, "Optical characterization and imaging of biological tissues," *Current Science*, Vol. 87, 218–227, 2004.
3. Byrne, D., M. O'Halloran, M. Glavin, and E. Jones, "Data independent radar beamforming algorithms for breast cancer detection," *Progress In Electromagnetic Research*, Vol. 107, 331–348, 2010.
4. O'Halloran, M., M. Glavin, and E. Jones, "Rotating antenna microwave imaging system for breast cancer detection," *Progress In Electromagnetic Research*, Vol. 107, 203–217, 2010.
5. O'Halloran, M., R. C. Conceicao, D. Byrne, M. Glavin, and E. Jones, "FDTD modeling of the breast: A review," *Progress In Electromagnetic Research B*, Vol. 18, 1–24, 2009.
6. Wilson, B. C. and S. L. Jacques, "Optical reflectance and transmittance of tissues: Principles and applications," *IEEE J. Quantum Electron.*, Vol. 26, 2186–2199, 1990.
7. Cui, W. and L. E. Ostrander, "The relationship of surface reflectance measurements to optical properties of layered biological media," *IEEE Trans. Biomed. Eng.*, Vol. 39, 194–201, 1992.
8. Singh, M. and S. Chacko, "Monte Carlo simulation of laser light scattering in mammalian organs," *Current Science*, Vol. 43, 1015–1019, 1997.
9. Chacko, S. and M. Singh, "Multi-layer imaging of human organs by measurement of laser backscattered radiation," *Med. Biol. Eng. Comput.*, Vol. 37, 278–284, 1999.
10. Kumar, D., S. Chacko, and M. Singh, "Monte Carlo simulation of

- photon scattering in biological tissue models,” *Indian J. Biochem. Biophys.*, Vol. 36, 330–336, 1999.
11. Warncke, D., E. Lewis, S. Lochmann, and M. Leahy, “A neural network based approach for determination of optical scattering and absorption coefficients in biological tissue,” *Journal of Physics, Conference Series*, Vol. 178, 012047, 2009.
 12. Chakrabarti, P., S. Kumar, P. Rout, and B. G. Rappai, “A proposed MISFET photodetector,” *Proceeding 3rd Asia Pacific Microwave Conference*, 575–578, Tokyo, Japan, 1990.
 13. Kabeer, M., K. Gowri, and V. Rajamani, “Three dimensional modeling and simulation of a nano MISFET photodetector,” *Journal of Optoelectronics and Advanced Materials*, Vol. 9, No. 9, 2879–2885, 2007.
 14. Pei, G., J. Kedzierski, P. Oldiges, M. Jeong, and V. Chinchun Kan, “FinFET design considerations based on 3-D simulation and analytical modeling,” *IEEE Trans. Electron Devices*, Vol. 49, No. 8, 1411–1419, 2002.
 15. El Hamid, H. A., J. R. Guitart, V. Kilchytska, D. Flandre, and B. Iniguez, “A 3-D analytical physically based model for the subthreshold swing in undoped trigate FinFETs,” *IEEE Trans. Electron Devices*, Vol. 54, No. 9, 2487–2496, 2007.
 16. Yang, W., Z. Yu, and L. Tian, “Scaling theory for FinFETs based on 3-D effects investigation,” *IEEE Trans. Electron Devices*, Vol. 54, No. 5, 1140–1147, 2007.
 17. Shao, X. and Z. Yu, “Nanoscale FinFET simulation: A quasi-3D quantum mechanical model using NEGF,” *Solid-State Electronics*, Vol. 49, 1435–1445, 2005.
 18. De Marchi, L., F. Franze, and E. Baravelli, “Wavelet-based adaptive mesh generation for device simulation,” *Solid-State Electronics*, Vol. 50, 650–659, 2006.
 19. Krumholz, M. and L. P. B. Katehi, “MRTD: New time-domain schemes based on multiresolution analysis,” *IEEE Trans. Microwave Theory Tech.*, Vol. 44, 555–571, 1996.
 20. Tentzeris, M. and J. Harvey, “Time adaptive time-domain techniques for the design of microwave circuits,” *IEEE Microwave Guided Wave Lett.*, Vol. 9, 96–99, 1999.
 21. Toupikov, M. and G. Pan, “On nonlinear modeling of microwave devices using interpolating wavelets,” *IEEE Trans. Microwave Theory and Tech.*, Vol. 48, 500–509, 2000.
 22. Holmstron, M., “Solving hyperbolic PDE’s using interpolating wavelets,” *SIAM J. Sci. Comp.*, Vol. 21, 405–420, 1999.

23. Ramesh, R., M. Madheswaran, and K. Kannan, "Optical effects on the characteristics of a nanoscale FinFET," *Progress In Electromagnetic Research B*, Vol. 21, 235–255, 2010.
24. Moradi, H., M. Falahpour, H. H. Refai, P. G. LoPresti, and M. Atiquzzaman, "BER analysis of optical wireless signals through lognormal fading channels with perfect CSI," *17th International Conference on Telecommunications*, 493–497, 2010.
25. Zhu, X. and J. M. Kahn, "Performance bounds for coded free-space optical communications through atmospheric turbulence channels," *IEEE Trans. on Communications*, Vol. 51, No. 8, 1233–1239, 2003.
26. Zhu, X. and J. M. Kahn, "Free-space optical communication through atmospheric turbulence channels," *IEEE Trans. on Communications*, Vol. 50, No. 8, 1293–1300, 2002.
27. Letzepis, N., I. Holland, and W. Cowley, "The Gaussian free space optical MIMO channel with Q -ary pulse position modulation," *IEEE Trans. on Wireless Communications*, Vol. 7, No. 5, 1744–1753, 2008.